12-3-2020

Epithermal Mineralization of the Bonanza-Sandy Vein System, Masara Gold District, Mindanao, Philippines

Jilian Aira S. Gabo-Ratio

Alfred Elmer Buena

Barbie Ross B. Villaplaza

Betchaida D. Payot

Carla B. Dimalanta

See next page for additional authors

Authors

Jilian Aira S. Gabo-Ratio, Alfred Elmer Buena, Barbie Ross B. Villaplaza, Betchaida D. Payot, Carla B. Dimalanta, Karlo L. Queaño, Eric A. Andal, and Graciano P. Yumul Jr

Journal of Asian Earth Sciences: X 4 (2020) 100041

Contents lists available at ScienceDirect

Journal of Asian Earth Sciences: X

journal homepage: www.sciencedirect.com/journal/journal-of-asian-earth-sciences-x

Epithermal mineralization of the Bonanza-Sandy vein system, Masara Gold District, Mindanao, Philippines

Jillian Aira Gabo-Ratio [a,*], Alfred Elmer Buena [a], Barbie Ross B. Villaplaza [a,b], Betchaida D. Payot [a], Carla B. Dimalanta [a], Karlo L. Queaño [c], Eric S. Andal [d], Graciano P. Yumul Jr. [e]

[a] Rushurgent Working Group, National Institute of Geological Sciences, College of Science, University of the Philippines, Diliman, Quezon City, Philippines
[b] Philsaga Mining Corporation, Upper Co-o, Bunawan, Agusan del Sur, Philippines[1]
[c] Department of Environmental Science, Ateneo de Manila University, Quezon City, Philippines
[d] Apex Mining Corporation, Inc., Ortigas Center, Pasig City, Philippines
[e] Cordillera Exploration Company, Inc., Bonifacio Global City, Taguig City, Philippines

ARTICLE INFO

Keywords:
Masara Gold District
Epithermal gold veins
Mindanao
Philippines

ABSTRACT

The Masara Gold District in southeastern Mindanao island is an area of prolific hydrothermal copper and gold mineralization. This study documents the mineralization characteristics of the NW-trending Bonanza-Sandy epithermal veins to constrain possible hydrothermal fluid sources and ore-forming mechanisms. Epithermal mineralization in the NW veins is divided into three main stages: Stage 1 - massive quartz-sulfide; Stage 2 - massive to amorphous quartz-carbonate (calcite); and Stage 3 - colloform-cockade quartz-carbonate (bladed rhodochrosite). Stage 1 is the main gold mineralization phase, with chalcopyrite, pyrite, sphalerite and galena occurring with native gold and tellurides. Stages 2 and 3 contain invisible gold in the sphalerite, galena, pyrite and chalcopyrite. The deposit exhibits mineralization characteristics typical of intermediate sulfidation epithermal deposits based on the dominant chalcopyrite-pyrite mineral assemblage; illite-muscovite-chlorite alteration mineralogy that point to neutral pH conditions; and sphalerite composition of 2.26 to 8.72 mol% FeS in Stage 1 and 0.55 to 1.13 mol% FeS in Stage 2. The K-Ar age date of illite separates from highly altered diorite porphyry of the Lamingag Intrusive Complex yielded an Early Pliocene age (5.12 ± 0.16 Ma). Hydrothermal fluid exsolved from the magma that formed the Lamingag Intrusive Complex probably formed the ore-forming Stage 1 veins. Stages 2 and 3 involved the deposition of quartz and carbonate veins possibly by boiling hydrothermal fluids. Precious and base metal deposition was controlled by the Masara Fault Zone. Exploration markers for gold mineralization in the Masara Gold District and vicinity include the presence of Lamingag Intrusive Complex and massive sulfide veins.

1. Introduction

The Philippines hosts world-class epithermal lode gold deposits found throughout the archipelago (Mitchell and Leach, 1991; Malihan et al., 2015). The majority of gold endowment in the Philippines has been produced from five major gold districts, including Baguio-Mankayan in northern Luzon, Paracale and Masbate in Bicol, and Surigao and Masara in Mindanao (Fig. 1A) (Mitchell and Leach, 1991; Yumul et al., 2003). These districts are within 515 km to the 1200-km long sinistral strike-slip Philippine Fault Zone (Mitchell and Leach, 1991).

Among these districts, the Baguio-Mankayan Gold District (Fig. 1A) in north Luzon is the most studied area (e.g. Cooke et al., 2011; Waters et al., 2011; Yumul et al., 2020), with studies of world class deposits of the Acupan-Sangilo (Cooke et al., 1996; Jabagat et al., 2020), Black Mountain (Cao et al., 2018), Sto. Tomas II (Imai, 2001; Masangcay et al., 2018) and the Lepanto-Far Southeast-Victoria systems (e.g. Arribas et al., 1995; Hedenquist et al., 1998; 2017; Imai, 2000; Claveria, 2001; Manalo et al., 2018). In contrast, the Masara Gold District in Mindanao island is considered to be one of the least studied in terms of mineralization characteristics. Recent publications describe the geology, structures, geophysics, geochemistry and alteration in the area (Malihan

* Corresponding author.
E-mail address: jgratio@nigs.upd.edu.ph (J.A. Gabo-Ratio).
[1] Now with.

https://doi.org/10.1016/j.jaesx.2020.100041

Available online 3 December 2020

et al., 2015; Manalo et al., 2017; Villaplaza et al., 2017; Yumul et al., 2017; Buena et al., 2019; Yumul et al., 2020). This paper examines the ore-gangue mineralogy, textures, nature of the ore-forming fluids, and the mechanisms of ore formation for the northwest-trending Bonanza-Sandy Au-bearing veins currently being mined by the Apex Mining Co., Inc. (AMCI) in the Masara Gold District. In addition to the vein samples collected, illite mineral separates from the wall rock were dated by the K-Ar method. The mineralization model proposed in this study may serve as a guide in the exploration of other potential mineralization in the vicinity.

2. Geologic framework

2.1. Regional geology

The Philippines is bound by subduction systems of opposing dips (Fig. 1A). To the west are the Manila Trench, Negros-Sulu Trench and Cotabato Trench, with subduction of the South China Sea, Sulu Sea and Celebes Sea basins, respectively. To the east is the East Luzon Trough-Philippine Trench system, which consumes the West Philippine Sea basin. The kinematic interactions between these subduction zones led to the formation of the sinistral Philippine Fault Zone (PFZ) in the Philippine Mobile Belt (PMB) (Galgana et al., 2007; Aurelio et al., 2013). The PFZ transects the entire archipelago and majority of the mineralized areas (i.e., the gold districts of Baguio-Mankayan in Northern Luzon, Paracale in Bicol Peninsula, Masbate island, and Surigao and Masara in Mindanao) (Fig. 1A).

Eastern Mindanao (Pacific Cordillera) is separated from Central Mindanao by the sinistral PFZ (Fig. 1B), bound by the Agusan-Davao Basin to the west and by the southern portion of the Philippine Trench to the east. Eastern Mindanao is underlain by a basement of Cretaceous ophiolitic fragments and metamorphosed rocks intruded by Oligocene to Plio-Pleistocene igneous rocks with early Miocene conglomerate, sandstone and limestone (Sajona et al., 1997; Suerte et al., 2009). Calc-alkaline and adakitic magmatism played a major role in the hydrothermal mineralization prolific in the area (e.g. Suerte et al., 2009; Sonntag et al., 2011; Yumul et al., 2017, 2020; Braxton et al., 2018). In Eastern Mindanao, the major hydrothermal systems include the Boyongan-Bayugo porphyry copper-gold deposit (e.g., Braxton et al., 2012; 2018) and the sedimentary rock-hosted Siana gold deposit in the Surigao District, the Co-O epithermal gold deposit in Agusan del Sur (e.g., Sonntag et al., 2011), the Diwalwal epithermal gold deposit in the Central District and the Masara epithermal gold and Kingking porphyry copper deposits in the Masara District (e.g., Suerte et al., 2009; Yumul et al., 2020) (Fig. 1B).

2.2. Masara Gold District

The Masara Gold District in the southern portion of Eastern Mindanao is known for prolific gold and copper mineralization. It is situated in a dilational jog of the Philippine Fault Zone within caldera structures, and hosts the Masara-Hijo-Amacan copper gold deposits (Malihan and Flores, 2012; Yumul et al., 2017). The geologic units were investigated in detail by Buena et al. (2019), building on the initial works of Lodrigueza and Estoque (1976) and Mercado et al. (1987). The district is underlain by the Eocene Masara Formation, consisting of tuff deposits intercalated with andesite flows. This basement unit is unconformably overlain by the Miocene biohermal Agtuuganon Limestone. Various

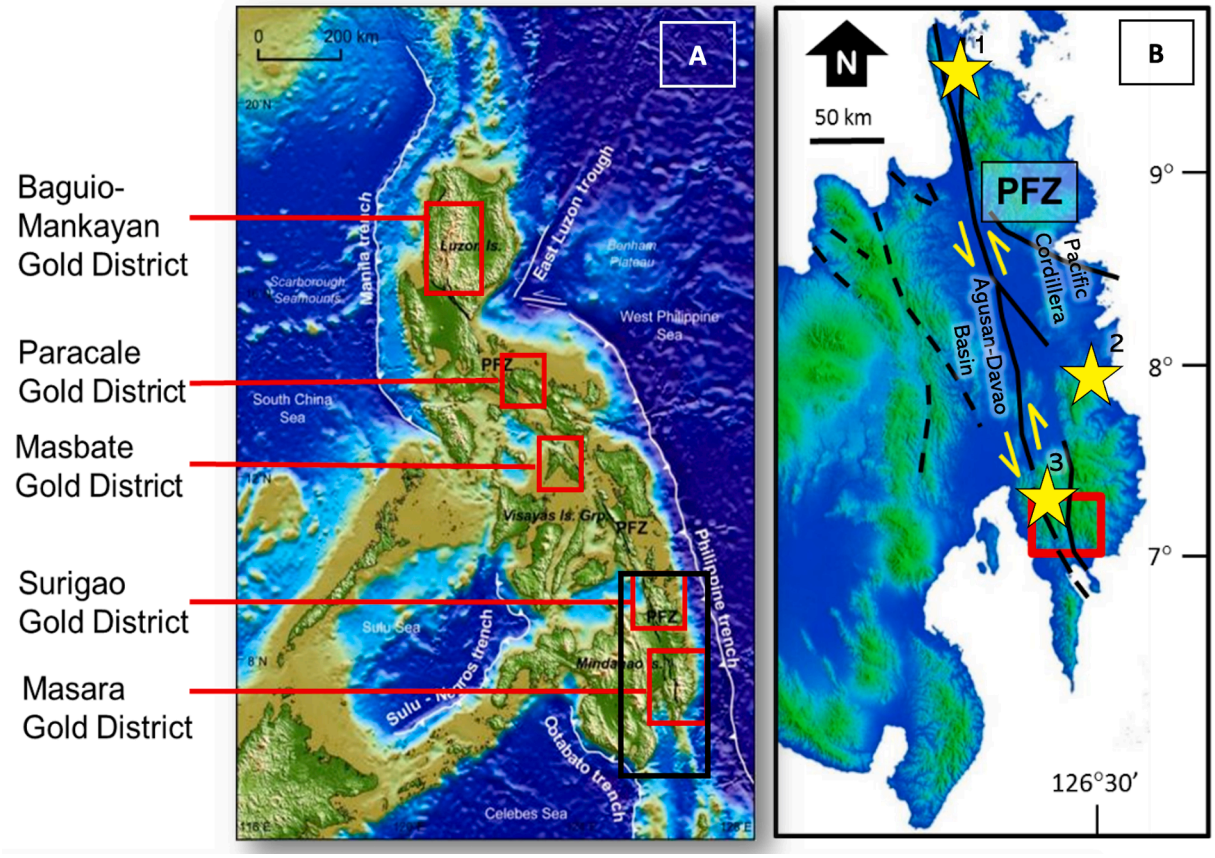

Fig. 1. A.) Location map showing the major gold districts (red boxes) in the Philippines (Mitchell and Leach, 1991). The black box in the southeastern portion represents the area shown in B. B.) Eastern Mindanao (Pacific Cordillera) being separated from the Agusan-Davao Basin by the Philippine Fault Zone. The yellow stars represent the major hydrothermal systems in Eastern Mindanao: 1) Boyongan-Bayugo deposit in the Surigao District; 2) Co-O epithermal deposit; and 3) Masara epithermal gold and Kingking porphyry copper deposits in the Masara District. The red box in B represents the location of the Masara Gold District as shown in Fig. 2.

stocks of intrusive units cut these older rocks. The Early Miocene equigranular Cateel Quartz Diorite is the dominant pluton in the area, subsequently intruded by the Middle Miocene plagiophyric dikes of the Alipao Andesite, followed by the Lamingag Intrusive Complex. The Intrusive Complex is composed of multiple stages of intrusion of quartz diorite stock, hypabyssal andesite and diorite porphyry. Our work, as will be shown later, shows that the Lamingag Intrusive Complex extends to a younger age. The youngest unit in the area is the Pliocene to Recent Amacan Volcanic Complex, which is composed of dacite lava and pyroclastic deposits.

These rock units record an evolution from tholeiitic magmatism (Masara Formation) due to the subduction of the proto-Molucca Sea Plate in the Eocene, to calc-alkaline Cateel Quartz Diorite in the Early Miocene (Yumul et al., 2017; Buena et al., 2019). Eastern Mindanao is postulated to have collided with a paleo-island arc in the Early to Middle Miocene, resulting in the deposition of the Agtuuganon Limestone and

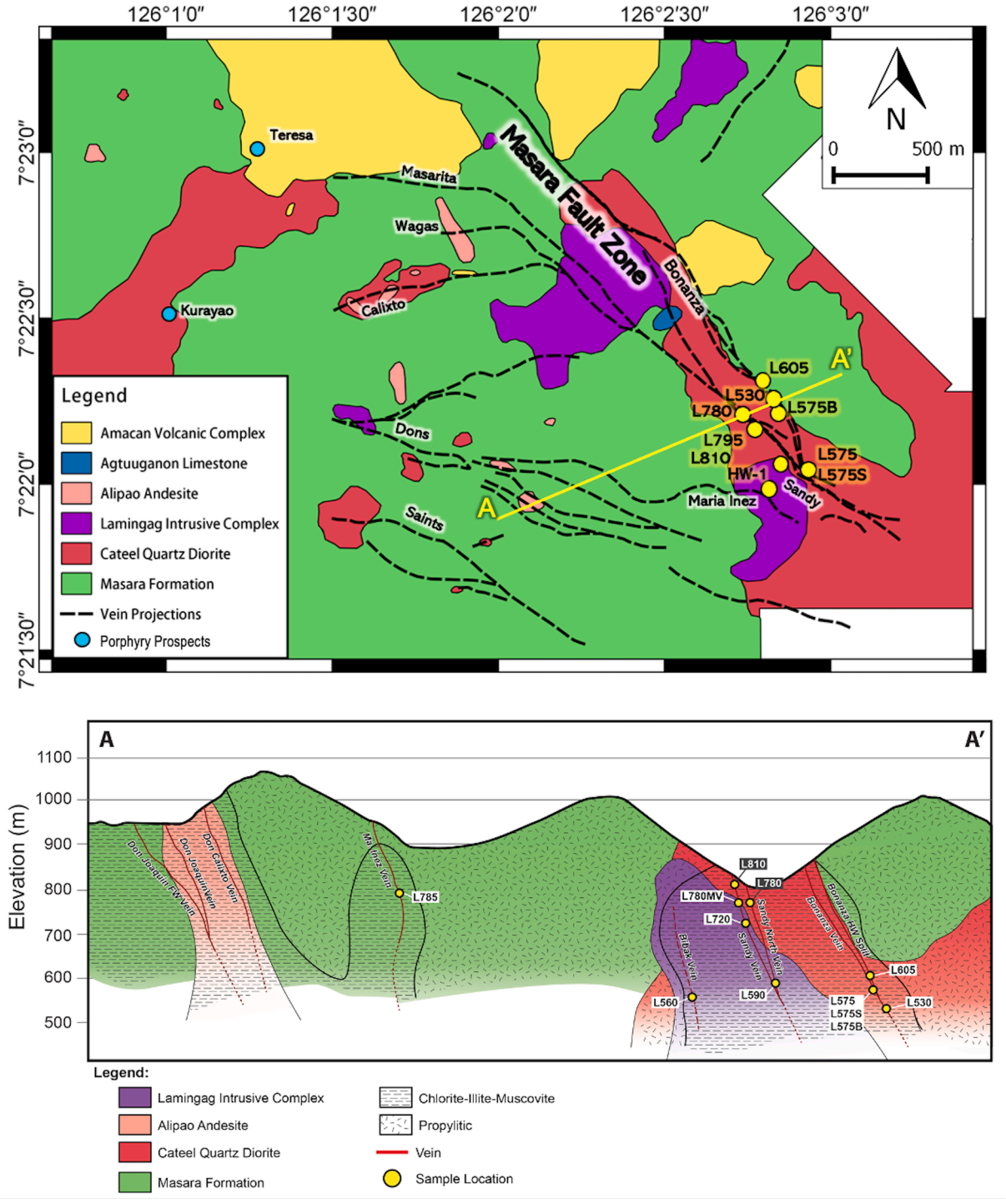

Fig. 2. Geologic map and cross-section of the Masara Gold District showing the distribution of the rock units (modified from Malihan et al., 2015; Buena et al., 2019). The mineralized zones are associated with NW- and EW-trending epithermal veins, whereas porphyry mineralization occurs at Teresa and Kurayao (blue circles). The yellow circles on the map are the surface projection of representative samples from the different mine levels, whereas those on the cross-section represent the sample location. (For interpretation of the references to colour in this figure legend, the reader is referred to the web version of this article.)

weak magmatism represented by the Alipao Andesite. The Late Miocene multiple dikes and stocks of the Lamingag Intrusive Complex represent reactivation of calc-alkaline magmatic activity and initial adakitic magmatism attributed to the onset of the eastward subduction of the Molucca Sea Plate. The Plio-Pleistocene unmineralized Amacan Volcanic Complex is characterized by adakitic signatures (Yumul et al., 2017).

Hydrothermal mineralization and associated alteration are hosted in the units of the Masara Formation, Cateel Quartz Diorite, Alipao Andesite and the Lamingag Intrusive Complex (Fig. 2) (Malicdem and Peña, 1967; Mercado et al., 1987; Villaplaza et al., 2017; Buena et al., 2019). The Plio-Pleistocene Amacan Volcanic Complex post-dates gold mineralization in Masara (Yumul et al., 2017; Buena et al., 2019). At least three mineralization styles have been recognized in the Masara Gold District: epithermal gold-silver mineralization (NW- and EW-trending mineralized veins related to the Masara Fault Zone); porphyry-related copper–gold mineralization (e.g. Kurayao and Theresa prospects); and minor skarn mineralization (Malihan and Flores, 2012; Malihan et al., 2015; Yumul et al., 2020) (Fig. 2).

This study concentrated on the present mine operations of AMCI, which are focused on the NW-trending gold-base metal epithermal veins (140 kt at 8.4 g/t Au, given a 3 g/t cutoff grade) (Malicdem and Peña, 1967; Mercado et al., 1987; Malihan and Flores, 2012). The NW-trending, NE-dipping mineralized faults serve as controls to the bonanza-grade epithermal mineralization (e.g., Bonanza-Sandy veins and their splits). The auxiliary E-W vein systems have associated WNW and ENE segmented trends of varying dip directions (e.g., veins in Wagas, Calixto, Dons and Saints), and are linked to the main NW-trending Masara Fault Zone as relay structures.

The recent work of Villaplaza et al. (2017) described at least five major alteration zones in the Masara gold district: (1) regional propylitic alteration zone; (2) potassic alteration zone with stockwork veins; (3) early-stage chlorite-illite-muscovite ± epidote alteration; (4) overprint of late-stage muscovite-illite ± chlorite alteration; and (5) minor occurrence of quartz + kaolinite + magnetite + dickite ± illite ± calcite localized along the Don Manuel Fault on the southwestern portion of the study area. The first three zones are linked to an earlier porphyry copper system in the Kurayao and Teresa areas (Fig. 2), whereas the late stage chlorite-illite-muscovite alteration in the eastern part are associated with the NW- and EW-trending epithermal gold veins.

A reinterpretation of the airborne magnetic survey in the area (Manalo et al., 2017) revealed magnetic low anomalies on the Reduced-to-Equator (RTE) map. These coincide with the location of the porphyry copper zones in Teresa and Kurayao. However, the early stage chlorite-illite-muscovite zone delineated by Villaplaza et al. (2017) coincides with the magnetic low RTE anomaly in the central portion of the Masara District. Considering the non-magnetic signature of this alteration zone, the observed anomaly must be caused by a deeper magnetic source. This is suggested to be the signature of the deeper magnetite-rich potassic alteration zone. It is further supported by the 500-meter upward continued magnetic anomaly map implying that a magnetic source is still present at ~250-meter depth (Manalo et al., 2017). Epithermal veins that reflect the Masara Fault Zone and the EW-trending faults in the central part of Masara display linear anomalies in the tilt derivative map.

3. Analytical techniques

3.1. Sampling methodology

Surface mapping and underground surveys were conducted in the NW-trending Bonanza and Sandy veins to identify occurrences of the epithermal veins, including ore and gangue mineralogy, sulfide abundance, textures and cross-cutting relationships. Approximately 30 vein samples were taken from the Bonanza and Sandy vein systems from the following mine levels corresponding to elevation (Fig. 2): L530, L575, L605, L780, L795 and L810.

3.2. Ore and gangue mineralogy and mineral chemistry

Petrography was conducted to establish ore mineral assemblage, textural relationships and paragenetic sequence. Double-polished, carbon-coated thin sections of vein samples were used for Electron Probe Micro Analysis (EPMA) using the JEOL JXA-8230 Super Probe at the University of the Philippines - National Institute of Geological Sciences (UP-NIGS). Elemental composition and abundances were measured using a Wave Dispersive Spectroscopy (WDS) analysis. Data obtained were calculated using the ZAF correction matrix from the JEOL software. Standard operating conditions for sulfide analysis were set at 20 kV acceleration voltage, 20nA beam current with a beam diameter of 5 μm. Results of the analysis yielded L-values which were processed for ZAF correction using the JEOL software. Data obtained from this calculation produced elemental abundances expressed in weight % (Reed, 1995). The detection limit per element varies per analysis and is calculated as a function of peak intensity and background intensity (Reed, 2000; Batanova et al., 2018). In this study, the detection limits were calculated to range from ~100–200 ppm.

3.3. K-Ar dating

The most illite-altered host rock in the immediate vicinity of the mineralized veins (Sample HW-1; Fig. 2) were dated by the potassium-argon (K-Ar) method, using illite separates to estimate the age of alteration. The diorite porphyry sample from the Lamingag Intrusive Complex was analyzed by the Hiruzen Institute for Geology and Geochronology, Co, Ltd., Okayama, Japan.

The rock sample was cut into one-centimeter thick rock slab then crushed to obtain 10–30 mesh size fractions. Illite was separated from the finer fractions following the mineral separation protocol reported by Yagi (2006). The fine-sized particles were extracted using an ultrasonic bath. The finer particles were extracted using a centrifuge and then dissolved by HCl to eliminate any presence of carbonates. The treated sample was viewed under the binocular microscope to have visual confirmation of illite (Yagi, 2006). The illite separates were analyzed for potassium content and argon isotopes. Qualitative analysis of potassium was carried out by flame photometry using a 2000 ppm Cs buffer within 2% analytical error. Further details of this analysis are reported by Nagao et al. (1984). For argon isotope analysis, the white mica samples were heated to 180–200 °C by ribbon and mantle heater for about 72 h to emit adsorbed gases under vacuum. The specimens that were wrapped in Al foil were vacuumed out at 180–200 °C for 3 days, then argon was extracted at 1500 °C in an ultra-high vacuum line. Calculations for the age at two-sigma confidence level were obtained following the methods described by Nagao et al. (1984) and Nagao and Itaya (1988). The decay constants for ^{40}K to ^{40}Ar and ^{40}Ca and ^{40}K content in potassium from Steiger and Jager (1977) were used in the age calculation for alteration/mineralization.

4. Results

4.1. NW-trending Bonanza-Sandy epithermal veins

The veins of the Masara Gold District are largely confined to the NW-trending Masara Fault Zone. This structure is characterized by continuous but segmented veins (e.g. Bonanza and Sandy veins) that split into minor branches (Fig. 2). The vein system is characterized by a complex history of multiple quartz-calcite-sulfide veins and hydrothermal breccias with late-stage carbonates (Fig. 3A-B). The Masara-Sandy veins strike northwest to west-southwest and dip steeply to the northeast. The vein system pinches and swells along its strike length, but thicknesses typically range from 0.5 to 1 m, with the thickest veins measuring >3 m. The vein phases are generally sulfide-rich, containing pyrite, chalcopyrite, sphalerite and galena, with high gold grades generally correlated with sulfide abundance. The veins exhibit open-space fill textures

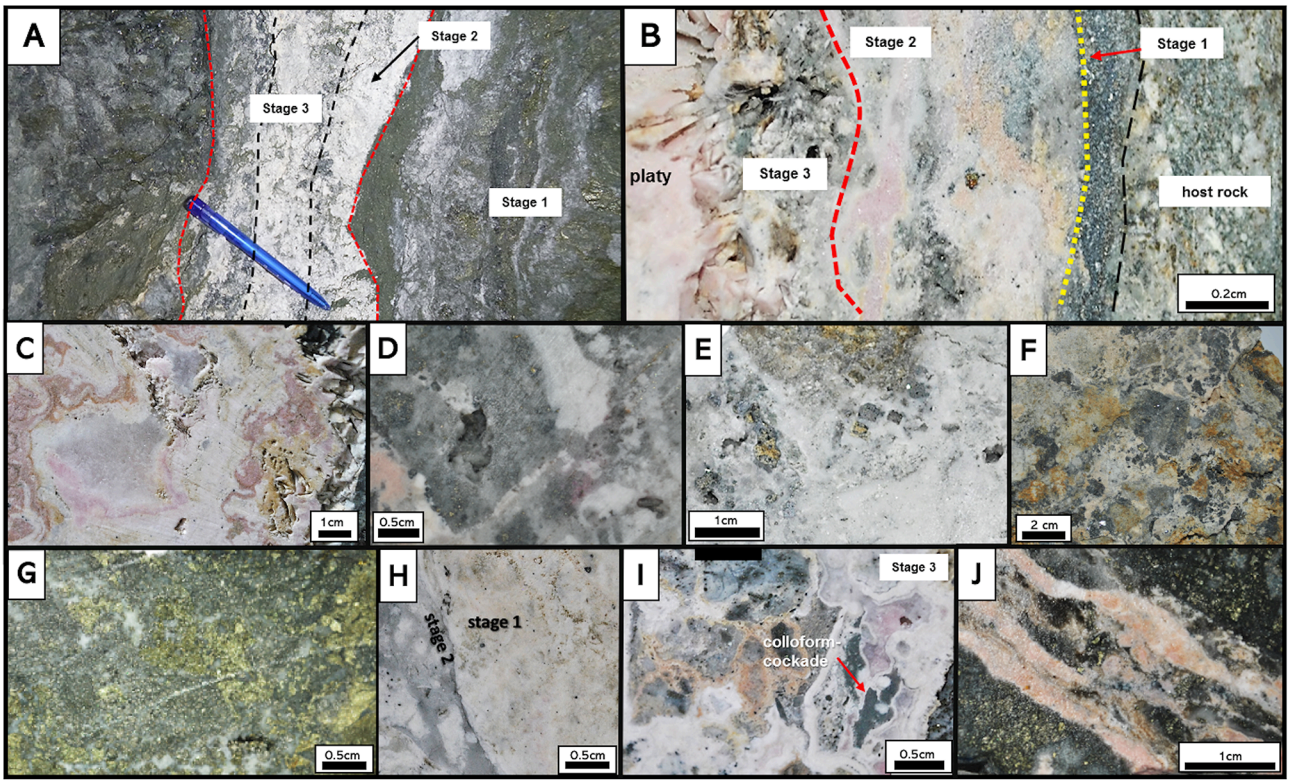

Fig. 3. A.) Representative underground exposure (Sample L810) of the NW-trending veins showing the cross-cutting relationships of Stages 1 to 3. B.) Detailed texture of the representative Masara epithermal veins exhibiting the three main paragenetic sequences (Sample L575S). C.) Colloform and bladed rhodochrosite with quartz of Stage 3 (Sample L575). D.) Stage 2 small quartz crystals exhibiting drusy texture (Sample L530). E.) Stage 2 drusy quartz associated with calcite and coarse-grained galena and sphalerite (Sample L795). F.) Stage 1 silicified breccia clasts in quartz-carbonate matrix (Sample L780) G.) Stage 1 massive sulfide vein exhibiting abundant chalcopyrite and pyrite with quartz and epidote (Sample L605). H.) Stage 2 vein (Sample L530) with massive to open-space quartz and calcite. I.) Stage 3 vein (Sample L575S) exhibiting colloform and cockade textures. J.) Stage 3 rhodochrosite veins cutting the Stage 1 massive sulfide veins (Sample L575S).

(crustiform, colloform, drusy and open space), brecciation (silicified breccia in quartz matrix) and selective replacement of carbonates by quartz (Fig. 3C-F). Alternating crustiform bands of sulfide and quartz-carbonate, as well as cockade and comb textures, indicate multiple mineralization pulses.

4.2. Ore-gangue mineralogy and vein paragenesis

From the ore and gangue mineral assemblage, textures and cross-cutting relationships of the NW-trending structures, three major stages of vein formation are identified (Fig. 3A-B, Table 1). Stage 1 occurs as

Table 1
Ore and alteration mineral paragenesis of the different stages of the Masara NW-trending epithermal veins. Thickness of the black lines indicates relative abundance; the solid red line refers to gold and telluride grains; red dashed line indicates invisible gold occurrence.

Paragenesis of the NW-trending Masara veins		*NW-trending system*		
		Stage 1	**Stage 2**	**Stage 3**
		Quartz sulfide	Quartz carbonate I	Quartz carbonate II
Mineralization	pyrite			
	chalcopyrite			
	galena			
	sphalerite			
	gold			
Ore Texture		massive, brecciated	massive, amorphous	colloform, crustiform, brecciated, platy
Alteration	quartz			
	calcite			
	rhodochrosite			
	illite			
	muscovite			
	chlorite			
	epidote			

massive sulfide vein with minor quartz and epidote (Fig. 3G), with anhedral coarse-grained chalcopyrite surrounding subhedral fine- to medium-grained pyrite (Fig. 4A). Within the chalcopyrite, medium-grained subhedral sphalerite and galena exhibit interpenetrating grain boundaries. Stage 1 is the main gold mineralization phase, where precious metals occur as inclusions in pyrite and galena. Gold occurs mostly as native gold that is 5 to 50 μm in size (Figs. 4B and 5) or as gold-silver tellurides (Fig. 4C) identified as petzite and hessite (Figs. 6 and 7).

Stage 2 consists of massive to open-space fill quartz-carbonate vein (Fig. 3H) that cuts the Stage 1 veins (Fig. 3B). The quartz associated with Stage 2 exhibits massive texture with coarse-grained subhedral to euhedral sphalerite and galena with interpenetrating boundaries (Fig. 4D). Minor amounts of fine-grained anhedral chalcopyrite and pyrite are sparse. Gold is not visible but was detected as a trace element in sphalerite and pyrite, as quantified in the EPMA (Tables 3 and 4).

Stage 3 is characterized by a quartz-carbonate phase dominated by rhodochrosite (Fig. 3B-C). Multiple bands of colloform-crustiform with cockade-brecciated textures are commonly observed in this stage (Fig. 3I-J), as well as rhodochrosite with platy textures (Fig. 3B-C). Anhedral coarse- to medium-grained sphalerite is the dominant sulfide phase, with minor fine-grained euhedral galena and pyrite and anhedral chalcopyrite (Fig. 4E). Stage 3 exhibits the same sulfide assemblage as Stage 2, but the sphalerite and galena grains are finer-grained with rare chalcopyrite and pyrite.

4.3. Alteration mineralogy

The paragenetic sequence determined for the three vein stages were incorporated with the observed alteration in the area following the study by Villaplaza et al. (2017) (Table 1). The NW-trending veins, especially Bonanza and Sandy, are dominantly hosted by altered intrusive bodies of the Cateel Quartz Diorite and Lamingag Intrusive Complex, and volcanic rocks of the Masara Formation (Fig. 2). Veins hosted in the intrusive units are typically thinner, whereas veins swell where hosted in the Masara Formation. Wall rocks immediately adjacent to the epithermal gold-base metal quartz veins of Stage 1 have halos of quartz + chlorite + illite + muscovite + pyrite ± epidote ± smectite ± adularia ± magnetite. Meanwhile, a later stage illite-muscovite alteration is mainly observed in rocks predominantly hosting the quartz-carbonate Stage 2 and 3 veins. This late-stage illite-muscovite alteration assemblage associated with the veins were observed to overprint an earlier alteration zone of quartz + chlorite + illite + muscovite + pyrite ± biotite ± smectite ± magnetite ± calcite, thought to be associated with an older porphyry copper–gold system in the Kurayao and Teresa areas

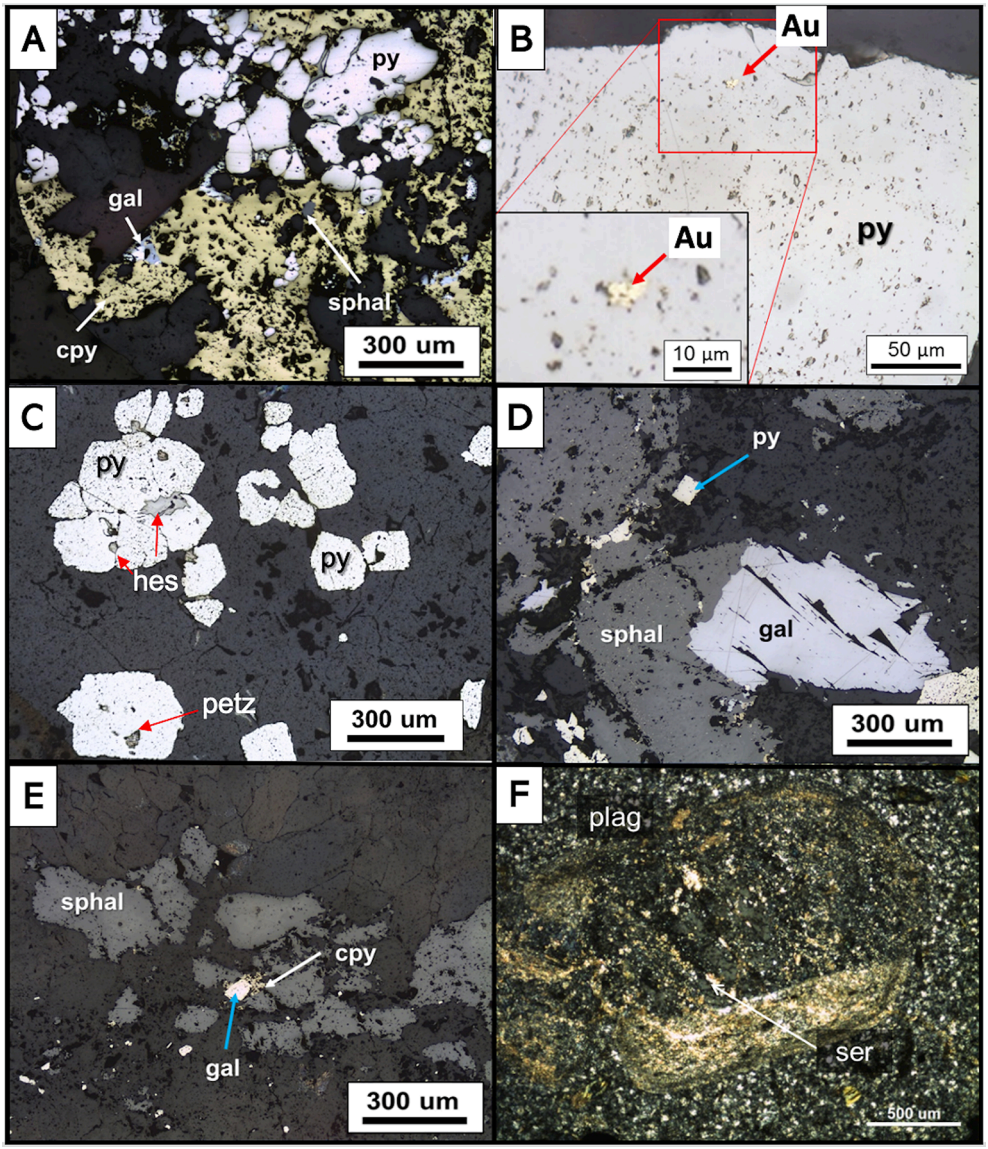

Fig. 4. A.) Stage 1 quartz-sulfide vein (Sample L605) containing chalcopyrite (cpy) and pyrite (py) as the dominant sulfide assemblage with minor disseminations of galena (gal) and sphalerite (sphal). B.) Native gold (Au) in pyrite found in Stage 1 vein (Sample L780) associated with the gold-silver tellurides. C.) Stage 1 veins (Sample L780) with hessite (hes) and petzite (petz) tellurides occurring as pyrite inclusions. D.) Stage 2 quartz-carbonate vein (Sample L575B) mostly containing sphalerite and galena with sparse distribution of pyrite. E.) Stage 3 quartz-carbonate vein (Sample L795) with sphalerite and minor occurrences of galena and chalcopyrite. F.) Photomicrograph of plagioclase altered to illite in the diorite porphyry unit of the LIC used for age dating (Sample HW-1).

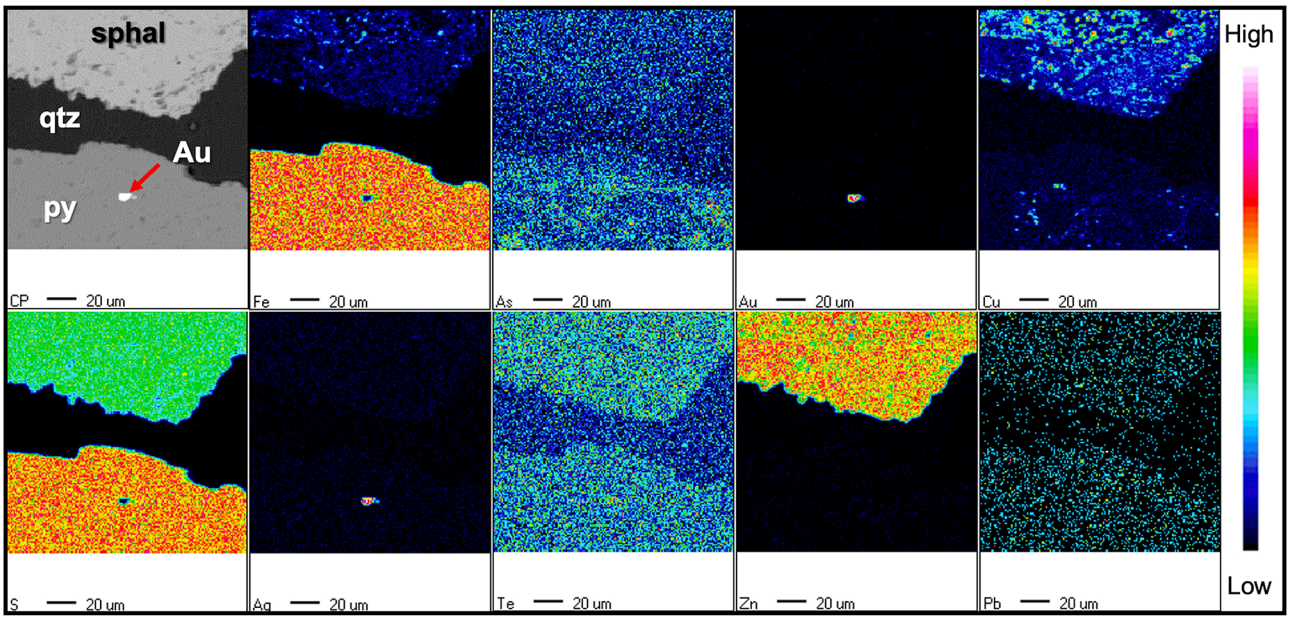

Fig. 5. Multi-element compositional map of Sample L780 shows peak in concentration of gold and silver (pink color) of the native gold grain (Au) included by pyrite (py). Microprobe analysis of the grain using Wave Dispersive Spectroscopy (WDS) yielded Au/Ag ratio of 5.7 at 85% Au and 15% Ag. CP-composite view, Fe-iron, As-arsenic, Au-gold, Cu-copper, S-sulfur, Ag-silver, Te, tellurium, Zn-zinc, Pb-lead, sphal – sphalerite, qtz - quartz.

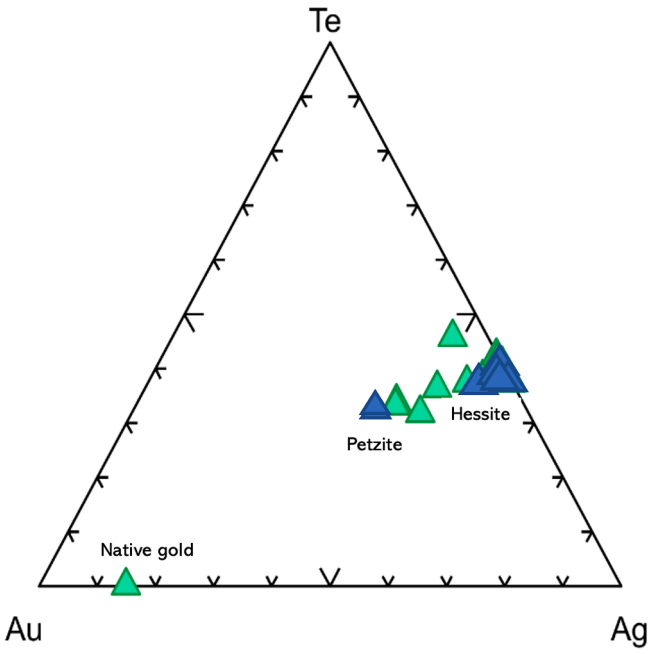

Fig. 6. Au-Te-Ag ternary system modified from Cabri (1965) showing the Stage 1 gold and telluride grains from sample L780 (green triangles) and the Stage 1 gold-silver tellurides of sample L605 (blue triangles). (For interpretation of the references to colour in this figure legend, the reader is referred to the web version of this article.)

(Villaplaza et al., 2017).

The degree of host rock alteration varies from the immediate host rock towards the periphery of the veins. Higher degrees of alteration by chlorite-illite-muscovite occur proximal to the vein. Hornblende of the diorite units of both the Lamingag Intrusive Complex and the Cateel Quartz Diorite are partially to completely replaced by chlorite, and plagioclase is typically replaced by minor patches of illite and muscovite (Fig. 4F), and locally calcite. Where the veins are hosted in the diorite porphyry unit of the Lamingag Intrusive Complex, sericitization is most prevalent. A few meters from the vein, regional propylitic alteration dominates.

4.4. Mineral chemistry

4.4.1. Gold and tellurides

Mineral chemistry analysis of the native gold grain yielded elemental compositions of 85% Au and 15% Ag, a ratio of 5.7 (Figs. 5 and 6). Quantitative analysis of 30 gold-silver telluride grains included by pyrite and chalcopyrite in Stage 1 of sample L780 revealed hessite (Ag_2Te) as the dominant gold-silver telluride phase with minor occurrences of petzite (Ag_3AuTe_2) (Table 2, Figs. 6 and 7). Analysis of 15 telluride grains included in pyrite and chalcopyrite in the Stage 1 vein of sample L605 also identified hessite and petzite.

4.4.2. Sphalerite

Sphalerite grains that coexist with pyrite in Stages 1 and 2 have core compositions with higher Fe (1.50–5.99 wt%) in Stage 1 than Stage 2 sphalerite (0.38–0.74 wt%) (Table 3). Stage 1 sphalerite grains also exhibit higher Cu content (1.53–6.16 wt%) compared to Stage 2 (nil concentrations of Cu in most grains except for one at 0.27 wt%).

The mole % Fes of the sphalerite grains for each stage revealed Stage 1 values of 3.4 to 9.8 mol% FeS for sample L575, 2.3 to 2.5 mol% Fes for sample L605 and 3.91 to 8.72 mol% FeS for sample L780 (Table 3). The sphalerites from Sample L780 representing Stage 2 contain 0.55 to 1.13 mol% FeS; mol% FeS of Stage 3 sphalerite was not possible. Significant total values were not obtained for the sphalerites of this stage.

4.4.3. Pyrite

In several Stage 1 pyrites, gold is detected as invisible gold in-lattice and ranges from 0.01 to 0.04 wt% (100–400 ppm) content (Table 4). The gold also occurs as native gold, petzite and hessite telluride inclusions. In Stage 2, gold was detected as invisible gold in the pyrite, galena and sphalerite, ranging from 0.01 to 0.03 wt% (100–300 ppm). Only one grain from Stage 3 had detectable gold content at 0.01 wt% (100 ppm).

The trace element content in pyrite from the three stages determined that Co content ranges from 0.07 to 0.10 wt% for Stage 1, 0.09–0.11 wt % for Stage 2, and 0.11–0.14 wt% for Stage 3 (Table 4).

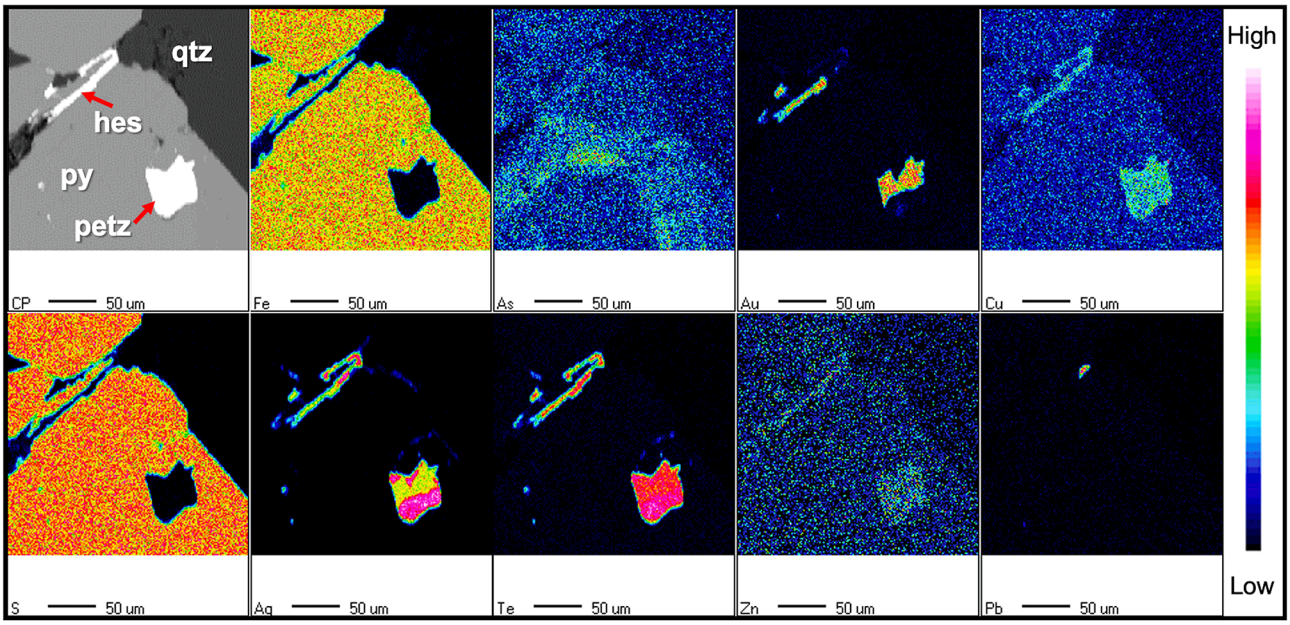

Fig. 7. Representative multi-element compositional map of Sample L780 showing tellurides hosted in pyrite (py) with peak concentration in Ag, Au and Te (pink colors). The tellurides were identified as hessite (hes) and petzite (petz) from WDS analyses (Table 2). CP-composite view, Fe-iron, As- arsenic, Au-gold, Cu-copper, S-sulfur, Ag-silver, Te, tellurium, Zn-zinc, Pb-lead, sphal-sphalerite, qtz-quartz.

4.5. K-Ar dating

White mica alteration of host rocks is cut by the NW-trending epithermal veins and is used to approximate the timing of epithermal mineralization (e.g., Arribas et al., 1995; Tassinari et al., 2008). Illite separates from the diorite porphyry (Fig. 4F) of the Lamingag Intrusive Complex (Sample HW-1, Fig. 2) yielded a K-Ar age of 5.12 ± 0.16 Ma (Early Pliocene) (Table 5).

5. Discussion

5.1. Ore-forming conditions

The alteration minerals associated with Stage 1 base metal veins are quartz and epidote with halos of quartz, chlorite, illite and muscovite (Table 1). Stages 2 and 3 quartz-calcite-rhodochrosite veins have halos of illite-muscovite. The alteration minerals in the NW-trending Masara epithermal deposit reveal typical neutral pH environment of formation. In addition, the temperature of formation of epidote is at 240–300 °C while illite and chlorite are estimated to form at ~220–300 °C in epithermal environments (Henley and Ellis, 1983; Reyes, 1990; Simmons et al., 2005). These temperatures may be roughly inferred to be the conditions during vein deposition.

Stage 1 veins are dominated by massive sulfide and quartz associated with chalcopyrite and pyrite with galena and sphalerite. Gold mineralization in the NW-trending vein system occurs as native Au and gold-silver tellurides in Stage 1 massive sulfide veins, which suggests an influence of a magmatic source of Te (e.g. Gao et al., 2015). Stage 2 consists of massive to open-space fill quartz-carbonate with galena and sphalerite along with minor pyrite and chalcopyrite. Stage 3 exhibits colloform bands and bladed rhodochrosite with sphalerite, galena and chalcopyrite as the primary minerals. The textures exhibited by Stage 3 indicate boiling as a possible mechanism for deposition (Dong et al., 1995). For Stages 2 and 3, gold is commonly invisible, which refers to the nonstructural ultramicroscopic and structurally-bound isomorphic states of gold (Vikentyev, 2015). This is represented as submicron to nanoscale inclusions of gold in sulfides (e.g. Tauson et al., 1998; Deditius et al., 2014), possibly due to gold substituting for arsenic in the iron sites of pyrite crystal structures (Boyle, 1979; Cook and Chryssoulis, 1990). In both stages, gold composition is up to 0.03% within the sphalerite and pyrite minerals (Tables 3 and 4).

5.2. Sulfidation state and mineralization style

The sulfidation state can be identified based on temperature of formation (estimated here from alteration mineralogy) and mol% FeS in sphalerite grains (Barton, 1970; Czamanske, 1974; Einaudi et al., 2003) (Fig. 8). In this study, Stage 1 veins are dominantly composed of chalcopyrite and pyrite with galena and sphalerite. Chalcopyrite and pyrite represent the upper and lower stability limit of intermediate sulfidation state, respectively. Sphalerite grains from Stage 1 consist of 2.54 to 8.72 mol % FeS (Table 2), consistent with an intermediate sulfidation state at epithermal temperatures (Einaudi et al., 2003).

Stage 2 quartz-carbonate veins (Table 1) consist mostly of sphalerite and galena with minor chalcopyrite and pyrite. Sphalerite from this stage has 0.55 to 1.13 mol % FeS, which corresponds to the upper portion of intermediate sulfidation state (Einaudi et al., 2003) (Fig. 8). Both Stages 1 and 2 veins of the NW-trending Masara epithermal veins conform to the typical fluid evolutionary path of base-metal veins (Fig. 8).

Stage 3 veins are characterized by abundant rhodochrosite, common in intermediate sulfidation deposits (Hedenquist et al., 2000; Wang et al., 2019); there is no sphalerite in this stage. The alteration minerals muscovite, illite and chlorite in the Masara Gold District NW-trending veins (Villaplaza et al., 2017) are consistent with intermediate sulfidation characteristics that formed at near-neutral pH conditions (Hedenquist et al., 2000).

The Masara Gold District formed during arc magmatism, with neutral to compressive stress regime in the study area typically associated with porphyry Cu and associated high-sulfidation and intermediate-sulfidation epithermal Au deposits (Einaudi et al., 2003; Wang et al., 2019). The tectonic regime, combined with ore-gangue mineralogy, sulfidation state and alteration mineralogy, indicates an intermediate sulfidation style of epithermal mineralization for the NW-trending veins of the Masara deposit.

Table 2
Summary of gold and tellurides mineral chemistry analysis from Sample L780 and L605 Stage 1 veins. '–' means below detection limit. Minimum detection limits are 0.01–0.02 wt% for all elements.

L780 wt.%	C0-1	C0-2	C0-3	C11-4	C1-3	C1-4	C1-5	C1-6	C1-7	C1-10	C1-11	C1-12	C2-1	C2-2	C2-4
Ag	61.68	59.23	57.95	55.48	59.14	62.72	60.50	60.77	63.62	59.17	57.65	59.80	58.39	58.80	44.95
Au	0.03	0.37	0.29	7.88	1.13	–	–	–	0.09	0.08	4.62	0.01	0.26	0.45	21.83
Bi	0.01	0.04	–	0.04	0.01	0.03	–	0.03	0.01	0.02	0.10	–	0.02	0.02	0.38
Co	–	–	0.01	–	–	–	–	0.01	0.01	–	–	0.02	–	–	0.01
Cu	–	–	0.03	0.02	0.03	0.07	–	0.08	0.07	0.09	0.01	0.25	0.04	0.01	0.01
Fe	0.59	0.17	0.72	0.50	0.45	0.57	0.31	0.26	0.01	0.82	0.14	0.12	0.20	0.39	0.93
Ni	–	–	–	–	–	0.08	–	–	–	–	–	–	–	–	–
S	0.17	0.07	0.34	0.14	0.26	0.12	0.12	0.14	0.11	0.17	0.10	0.15	0.18	0.21	0.15
Se	–	–	–	–	–	–	–	–	0.00	0.14	–	0.02	0.01	0.06	0.02
Te	40.45	41.70	42.25	37.65	40.47	38.54	39.49	40.77	38.85	40.67	38.68	41.26	43.01	42.03	34.12
Zn	0.02	–	0.12	0.05	0.06	0.06	–	0.03	0.02	–	0.13	0.07	0.00	0.05	0.04
Total	102.96	101.57	101.70	101.76	101.55	102.20	100.43	102.09	102.79	101.14	101.43	101.69	102.12	102.02	102.44
Mineral	Hessite	Hessite	Hessite	Hessite	Hessite	Hessite	Hessite	Hessite	Hessite	Hessite	Hessite	Hessite	Hessite	Hessite	Petzite

L780	C2-5	C2-6	C2-7	C2-8	C2-9	C11-1	C11-2	C11-4	C11-10	C11-12	C11-13	C11-15	C11-16	C11-17	C11-18
Ag	61.92	49.89	50.48	45.22	62.21	58.89	61.09	62.57	61.17	62.05	58.81	61.02	61.05	60.63	60.23
Au	0.04	18.76	13.49	22.45	0.13	0.84	0.83	0.05	0.74	0.65	0.50	0.72	0.08	0.63	1.09
Bi	0.03	0.28	0.18	0.16	0.02	0.03	0.04	0.04	0.03	0.02	0.01	0.00	–	–	0.07
Co	–	0.02	0.02	–	–	0.01	–	0.01	–	–	–	–	0.01	0.01	–
Cu	0.06	–	0.03	0.01	0.33	–	–	0.02	–	–	–	0.04	–	–	–
Fe	2.25	0.33	1.43	1.19	1.02	0.60	0.35	0.60	0.16	0.91	0.04	0.11	0.52	0.70	1.09
Ni	0.02	–	0.06	–	–	–	–	–	0.09	–	–	–	0.16	0.10	0.01
S	1.04	0.14	0.21	0.20	0.28	0.09	0.10	0.17	0.10	0.12	0.11	0.07	0.15	0.06	0.19
Se	0.01	0.02	0.04	–	0.04	0.07	–	0.01	–	0.04	–	0.00	–	–	0.02
Te	37.38	32.01	36.55	33.51	38.21	38.38	39.19	39.31	39.30	38.93	37.31	40.14	40.00	39.74	39.66
Zn	0.03	–	–	–	0.03	–	0.07	0.05	0.03	–	–	–	0.02	0.03	–
Total	102.77	101.43	102.47	102.74	102.27	98.91	101.68	102.82	101.62	102.71	96.77	102.09	101.99	101.90	102.35
Mineral	Hessite	Petzite	Petzite	Petzite	Hessite	Hessite	Hessite	Hessite	Hessite	Hessite	Hessite	Hessite	Hessite	Hessite	Hessite

L605	C2-1	C2-4	C2-5	C2-6	C2-7	C2-10	C2-11	C2-12	C2-13	C2-17	C2-18	C2-25	C2-29	C2-30	C2-33
Ag	59.10	40.95	41.45	41.06	61.60	58.59	56.52	59.34	59.82	59.86	57.74	59.11	61.65	58.51	53.85
Au	2.44	25.78	25.85	25.39	0.81	2.15	4.90	1.15	1.91	1.56	0.78	2.66	1.14	1.99	1.83
Co	–	0.01	–	0.01	0.01	0.01	0.01	0.01	0.00	0.00	0.00	0.00	0.00	0.01	0.01
Cu	–	0.05	–	0.00	0.04	0.13	0.29	0.03	0.02	1.13	0.00	0.02	0.14	0.12	0.02
Fe	0.55	0.35	0.12	0.15	0.25	1.23	0.34	1.93	1.14	0.72	0.36	0.78	0.38	1.32	6.56
S	0.38	0.14	0.11	0.13	0.21	0.51	0.57	0.93	0.13	0.12	0.16	0.56	0.38	0.49	6.94
Se	–	–	0.04	0.00	0.01	0.02	0.00	0.00	0.00	0.00	0.00	0.00	0.00	0.03	0.02
Te	37.49	31.98	32.95	32.95	37.03	37.22	35.66	36.60	38.05	37.18	38.54	37.40	37.32	37.43	33.17
Total	99.96	99.26	100.52	99.69	99.95	99.86	98.28	99.98	101.06	100.57	97.58	100.53	101.02	99.90	102.38
Mineral	Hessite	Petzite	Petzite	Petzite	Hessite	Hessite	Hessite	Hessite	Hessite	Hessite	Hessite	Hessite	Hessite	Hessite	Hessite

Table 3
Summary of sphalerite mineral chemistry analysis of Stage 1 and Stage 2 veins from L575, L605 and L780. '–' means below detection limit. Minimum detection limits are 0.01–0.02 wt% for all elements.

No.	L575-1	L575-2	L575-3	L605-1	L605-2	L780-1	L780-2	L780-3	L780-4	L780-5	L780-6	L780-7	L780-8	L780-9	L780-10
Stage	Stage 1			Stage 1		Stage 1					Stage 2				
(wt.%)															
Ag	–	–	–	–	–	–	–	–	–	–	–	–	–	–	–
Fe	2.23	3.16	5.99	1.5	1.68	3.56	2.38	2.9	4.53	5.33	0.44	0.39	0.74	0.37	0.38
S	33.57	33.27	33.96	33.36	33.46	33.72	33.66	33.65	34.38	34.31	33.56	33.56	33.56	33.41	33.53
Se	0.01	0.03	0.12	–	0.03	0.03	–	–	–	–	0.02	–	–	0.02	–
Cu	1.78	2.7	6.16	1.35	1.52	2.65	1.53	1.93	3.79	4.05	–	–	0.27	–	–
Zn	63.73	61.51	54.91	64.86	64.33	57.03	58.45	58.35	54.67	55.76	65.8	66.58	64.83	66.88	66.55
Au	–	–	–	–	0.04	–	–	0.02	–	–	–	–	–	–	0.03
Bi	–	–	–	–	–	–	0.02	–	0.04	0.02	–	–	–	–	0.03
Co	0.01	–	–	–	–	0.01	0.01	0.01	0.01	–	–	–	–	–	–
Te	–	–	–	–	–	–	0.01	–	–	–	–	–	–	–	–
Ni	–	–	0.01	–	0.01	0.01	–	–	0.01	–	–	–	–	–	–
Cd	0.21	0.22	0.21	0.23	0.23	0.18	0.17	0.16	0.17	0.18	0.46	0.39	0.23	0.47	0.44
Total	101.5	100. 9	101.4	101.3	101.3	97.2	96.2	97	97.6	99.7	100.3	100.9	99.6	101.2	101
FeS mol%	3.38	4.89	9.84	2.26	2.54	5.88	3.91	4.73	7.65	8.72	0.66	0.58	1.13	0.55	0.57

5.3. Mineralization model and implications for exploration

Integrating geologic and geochronological data with the nature of the mineralizing fluids and the ore-forming mechanisms, a mineralization model is proposed for the Masara Gold District NW-trending epithermal veins (Fig. 9). The Masara Gold District is underlain by the basement rock of the Eocene volcanic-pyroclastic basement of the Masara Formation, which is cut by the NW-trending Masara Fault

Table 4
Summary of pyrite mineral chemistry analysis from sample L780 containing Stage 1 and Stage 2 veins and sample L575 Stage 3 veins. '–' means below detection limit. Minimum detection limits are 0.01–0.02 wt% for all elements.

No.	L780-1	L780-2	L780-3	L780-4	L780-5	L780-6	L780-7	L780-8	L780-9	L780-10	L780-11	L780-12	L780-13	L780-14	L575-1	L575-2	L575-3	L575-4	L575-5	L575-6
Stage (wt%)	Stage 1							Stage 2							Stage 3					
Ag	–	0.01	–	0.002	–	–	0.01	–	–	–	–	–	0.033	0.017	0.02	–	–	0.01	–	0.02
Fe	47.5	47.3	47.25	47.21	47.05	46.68	46.37	47.21	47.32	47.25	47.31	46.88	46.53	46.62	47.25	47.2	46.72	46.97	46.27	47.86
S	54.2	54.31	54.22	53.5	53.57	54.09	54.03	53.69	53.55	53.49	53.64	53.45	54.27	54.16	53.83	53.71	54.32	53.96	52.7	53.8
Se	–	0.01	–	–	0.01	0.05	–	–	–	–	–	–	–	–	–	–	0.02	–	–	0.03
Cu	0.01	–	0.02	0.02	0.02	–	–	0.34	0.08	–	0.35	0.01	–	0.06	–	0.01	0.01	–	–	–
Zn	–	–	0.02	0.03	–	0.03	–	0.01	0.03	0.02	0.05	–	0.04	0.03	0.01	0	0.01	–	–	0.02
Au	–	0.02	0.01	0.02	0.01	–	0.04	0.03	0.01	–	0.02	0.02	–	0.02	0.01	–	–	–	–	–
Bi	–	0.02	–	–	0.02	0.05	–	–	0.01	0.03	–	0.05	0.04	0.02	–	–	–	–	–	–
Co	0.09	0.1	0.07	0.07	0.08	0.07	0.1	0.07	0.09	0.11	0.09	0.11	0.1	0.11	0.11	0.11	0.14	0.12	0.11	0.12
Te	0.03	0.01	0.01	0.03	0.04	–	–	–	–	–	–	–	0.02	–	–	0.01	–	–	0.01	–
Ni	–	–	–	–	–	–	–	0.003	–	–	–	–	–	–	0.01	–	–	–	–	–
Cd	0.01	0.02	0.01	0.02	0.02	0	–	–	–	–	–	–	–	0.04	0.001	0.01	0.03	–	0.02	0.01
Total	102	101.8	101.6	100.9	100.8	101	100.6	101.4	101.1	100.9	101.5	100.5	101	101.1	101.2	101.1	101.3	101.1	99.11	101.9

Table 5
K-Ar age from sericite separates from a highly altered diorite porphyry sample of the Lamingag Intrusive Complex.

Sample No.	Mineral (grain size)	K content (wt%)	Rad.^{40}Ar (10–8 cc STP/g)	K-Ar age (Ma)	Non-rad.^{40}Ar (%)
HW-1	Sericite (0.2–2.0 μm)	2.751 ± 0.055	54.682 ± 1.299	**5.115 ± 0.1586**	48

Zone (A in Fig. 9). After faulting, basement rocks were intruded by the pre-mineralization equigranular diorite stocks of the Cateel Quartz Diorite during the Early Miocene (B) along the Masara Fault Zone. Intrusion of the Middle Miocene porphyritic Alipao Andesite (C) followed, and then multiple stocks and dikes of the Late Miocene Lamingag Intrusive Complex (D). The latter intrusion is considered to be associated with mineralization (Buena et al., 2019), based on its close spatial and temporal association with epithermal veins.

The age of the illite-altered diorite porphyry host is 5.12 Ma (Early Pliocene), which coincided with the onset of formation of the Philippine Fault Zone in Mindanao (Quebral et al., 1996). This reactivated earlier-formed NW structures in southeastern Mindanao (Pubellier et al., 1994) such as the Masara Fault Zone, which eventually served as conduit for the mineralizing fluids to alter the diorite porphyry host and form the veins in the Masara Gold District.

The NW-trending Bonanza-Sandy veins exhibit intermediate sulfidation state characteristics. Stage 1 is characterized by massive quartz-sulfide veins with native gold and tellurides (E), consistent with a magmatic influence (e.g. Gao et al., 2015). During Stages 2 and 3, quartz and carbonate minerals deposited in veins (F). The colloform and crustiform plus platy textures exhibited by this stage (G in Fig. 9) point to the involvement of boiling.

In the Masara NW-trending veins, the sulfide-rich veins contain the highest grades of gold. Similar massive sulfide veins and textures in nearby structures may be indicators of mineralization. In the region, other occurrences of the Lamingag Intrusive Complex may provide exploration targets, as it was associated with mineralization, both temporally and spatially, of the NW-trending Bonanza-Sandy veins. Other Early Pliocene intrusive rocks in the region may also be prospective.

6. Conclusions

Mineralization in the NW-trending Bonanza-Sandy epithermal veins is hosted in the Masara Formation, Cateel Quartz Diorite and the Lamingag Intrusive Complex. The NW-trending epithermal veins in the Masara Gold District were formed in three major pulses which started during the Early Pliocene, or possibly earlier during the late Late Miocene: Stage 1 massive quartz-sulfide vein dominantly composed of pyrite, chalcopyrite, sphalerite and galena, with native gold, hessite and petzite; Stage 2 massive quartz carbonate vein composed of sphalerite, galena with minor pyrite and chalcopyrite; and Stage 3 colloform and crustiform quartz-carbonate (platy rhodochrosite) vein with sphalerite and minor galena and chalcopyrite.

The mineralization in the NW-trending Masara epithermal veins is attributed to late Late Miocene to Early Pliocene fluid circulation, which is temporally associated with the formation of the Philippine Fault Zone. The magmatic-hydrothermal fluid is possibly sourced from the Late Miocene Lamingag Intrusive Complex and eventually precipitated in the reactivated NW-trending Masara Fault Zone.

Exploration guides include massive sulfide veins and the presence of the Lamingag Intrusive Complex in the surrounding areas. In addition, the Early Pliocene rock units and structures in the vicinity of the Masara Gold District might also be worth looking into.

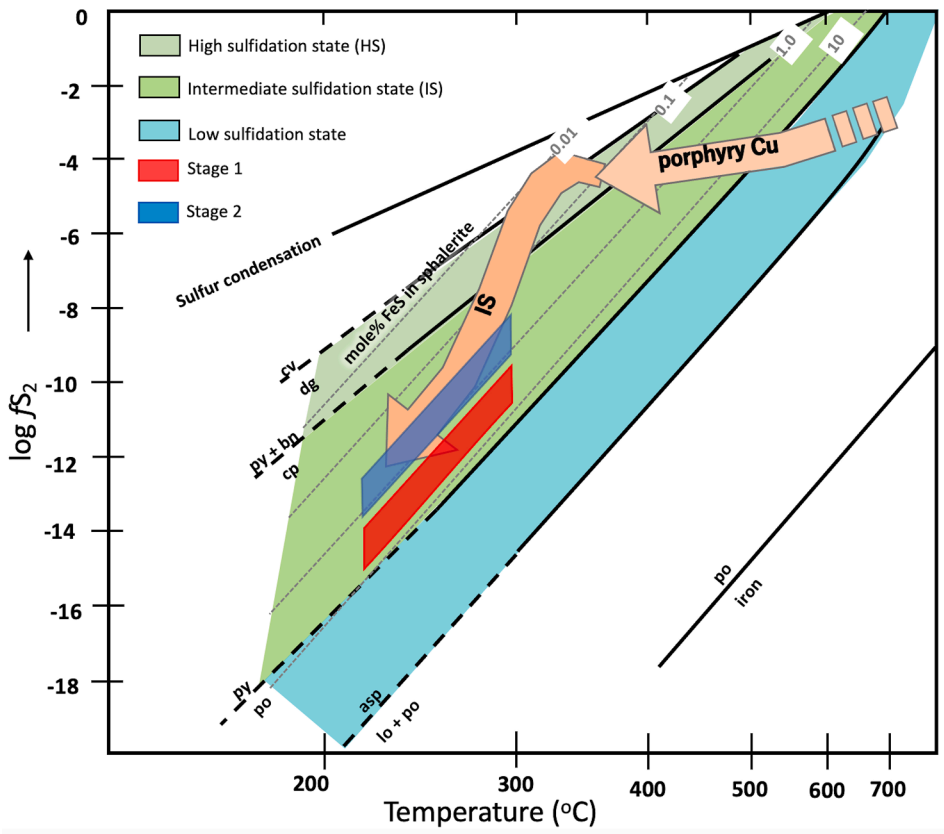

Fig. 8. Temperature vs sulfur fugacity diagram and the corresponding sulfide mineral assemblage showing the fields for Stage 1 and Stage 2 veins plotting in the intermediate sulfidation state. Temperatures were estimated from alteration minerals. Diagram modified from Einaudi et al. (2003), while the lines depicting mole% FeS in sphalerite are from Barton and Toulmin (1966). Also shown are paths depicting the evolution pathway of hydrothermal fluid associated with porphyry copper and intermediate sulfidation (IS) base-metal environment (light orange; from Einaudi et al., 2003). Cv-covellite; dg-digenite; py-pyrite; bn-bornite; cp-chalcopyrite; po-pyrrhotite; asp-arsenopyrite; lo-loellingite.

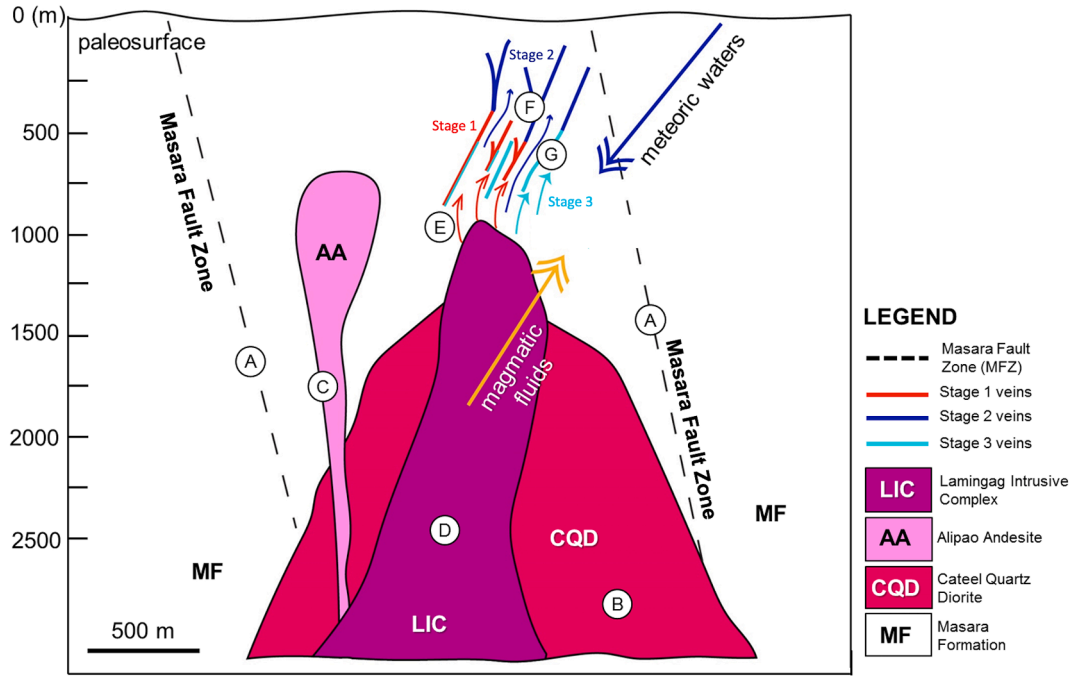

Fig. 9. Mineralization model of the NW-trending Masara Gold District showing the different intrusive units and the stages of mineralization represented by letters in circles: (A) Formation of the Masara Fault Zone; (B) intrusion of Cateel Quartz Diorite; (C) intrusion of the Alipao Andesite; (D) multiple intrusions of the Lamingag Intrusive Complex that resulted in hydrothermal fluid exsolution and circulation; (E) Stage 1 massive sulfide vein mineralization; (F) Stage 2 vein deposition; (G) Stage 3 vein formation.

CRediT authorship contribution statement

Jillian Aira Gabo-Ratio: Conceptualization, Methodology, Investigation, Formal analysis, Writing - original draft, Writing - review & editing, Visualization. **Alfred Elmer Buena:** Methodology, Investigation, Writing - original draft, Formal analysis, Visualization. **Barbie Ross B. Villaplaza:** Methodology, Investigation, Writing - review & editing, Visualization. **Betchaida D. Payot:** Writing - review & editing, Investigation, Methodology, Funding acquisition. **Carla B. Dimalanta:** Writing - original draft, Writing - review & editing, Investigation, Funding acquisition. **Karlo L. Queaño:** Investigation, Writing - review & editing, Visualization. **Eric S. Andal:** Investigation, Writing - review & editing, Resources. **Graciano P. Yumul:** Writing - original draft, Writing - review & editing, Investigation, Resources.

Declaration of Competing Interest

The authors declare that they have no known competing financial interests or personal relationships that could have appeared to influence the work reported in this paper.

Acknowledgments

This study forms part of the United States Agency for International Development through the Science, Technology, Research, and Innovation for Development (USAID STRIDE) research grant (Grant No. 0213997-G-2015-019-00). Logistical support provided by Apex Mining Co., Inc. (AMCI) and the University of the Philippines - National Institute of Geological Sciences (UP-NIGS) are gratefully acknowledged. The EPMA at the UP-NIGS was procured through a Department of Science and Technology grant. The support of Mr. Macky Barrientos in preparing tables and figures is also gratefully acknowledged. The comments of an anonymous reviewer and the significant inputs of Dr. Jeffrey Hedenquist are greatly appreciated.

References

Arribas Jr., A., Hedenquist, J.W., Itaya, T., Okada, T., Concepcion, R.A., Garcia Jr., J.S., 1995. Contemporaneous formation of adjacent porphyry and epithermal Cu-Au deposits over 300 ka in northern Luzon, Philippines. Geology 23, 337–340.

Aurelio, M.A., Peña, R.E., Taguibao, K.J.L., 2013. Sculpting the Philippine archipelago since the Cretaceous through rifting, oceanic spreading, subduction, obduction, collision and strike-slip faulting: Contribution to IGMA5000. J. Asian Earth Sci. 72, 102–107.

Barton, P.B., Jr. 1970. Sulfide petrology. Mineralogical Society of America, Special Paper No. 3, 187–198.

Barton, P.B., Toulmin, P., 1966. Phase relations involving sphalerite in the Fe-Zn-S system. Econ. Geol. 61, 815–849.

Batanova, V.G., Sobolev, A.V., Magnin, V., 2018. Trace element analysis by EPMA in geosciences: detection limit, precision and accuracy. IOP Conf. Series: Mater. Sci. Eng. 304, 012001.

Boyle, R.W., 1979. The geochemistry of gold and its deposits. Geol. Surv. Canada Bull. 280.

Braxton, D.P., Cooke, D.R., Dunlap, J., Norman, M., Reiners, P., Stein, H., Waters, P., 2012. From crucible to graben in 2.3 Ma: A high-resolution geochronological study of porphyry life cycles, Boyongan-Bayugo copper-gold deposits, Philippines. Geology 40, 471–474.

Braxton, D.P., Cooke, D.R., Ignacio, A.M., Waters, P.J., 2018. Geology of the Boyongan and Bayugo porphyry Cu-Au deposits: an emerging porphyry district in Northeast Mindanao, Philippines. Econ. Geol. 113 (1), 83–131.

Buena, A.E., Villaplaza, B.R.B., Payot, B.D., Gabo-Ratio, J.A.S., Ramos, N.T., Faustino-Eslava, D.V., Queaño, K.L., Dimalanta, C.B., Padrones, J.T., Tani, K., Brown, W.W., Yumul Jr., G.P., 2019. An evolving subduction-related magmatic system in the Masara Gold District, Eastern Mindanao, Philippines. J. Asian Earth Sci.: X 1, 100007.

Cabri, L.J., 1965. Phase relations in the Au-Ag-Te system and their mineralogical significance. Econ. Geol. 60, 1569–1606.

Cao, M., Hollings, P., Cooke, D.R., Evans, N.J., McInnes, B.I.A., Qin, K., Baker, M., 2018. Physicochemical processes in the magma chamber under the Black Mountain porphyry Cu-Au deposit, Philippines: Insights from mineral chemistry and implications for mineralization. Econ. Geol. 113, 63–82.

Claveria, R.J.R., 2001. Mineral paragenesis of the Lepanto copper and gold and the Victoria gold deposits, Mankayan mineral district, Philippines. Resource Geol. 51 (2), 97–106.

Cook, N.J., Chryssoulis, S.L., 1990. Concentrations of "Invisible Gold" in the common sulfides. Can. Mineral. 28, 1–16.

Cooke, D.R., McPhail, D.C., Bloom, M.S., 1996. Epithermal gold mineralization, Acupan, Baguio District, Philippines; geology, mineralization, alteration, and the thermochemical environment of ore deposition. Econ. Geol. 91, 243–272.

Cooke, D.R., Deyell, C.L., Waters, P.J., Gonzales, R.I., Zaw, K., 2011. Evidence for magmatic-hydrothermal fluids and ore-forming processes in epithermal and porphyry deposits of the Baguio district, Philippines. Econ. Geol. 106, 1399–1424.

Czamanske, G.K., 1974. The FeS content of sphalerite along the chalcopyrite-pyrite-bornite sulfur fugacity buffer. Econ. Geol. 69, 1328–1334.

Deditius, A.P., Reich, M., Kesler, S.E., 2014. The coupled geochemistry of Au and As in pyrite from hydrothermal ore deposits. Geochim. Cosmochim. Acta 140, 644–670.

Dong, G., Morrison, G., Jaireth, S., 1995. Quartz textures in epithermal veins, Queensland; Classification, origin and implication. Econ. Geol. 90, 1841–1856.

Einaudi, M.T., Hedenquist, J.W., Inan, E.E., 2003. Sulfidation state of fluids in active and extinct hydrothermal systems: Transitions from porphyry to epithermal environments. Soc. Econ. Geol. Special Publ. 10, 285–314.

Galgana, G., Hamburger, M., McCaffrey, R., Corpuz, E., Chen, Q., 2007. Analysis of crustal deformation in Luzon, Philippines using geodetic observations and earthquake focal mechanisms. Tectonophysics 432 (1–4), 63–87.

Gao, S., Xu, H., Zhang, D., Shao, H., Quan, S., 2015. Ore petrography and chemistry of the tellurides from the Dongping gold deposit, Hebei Province, China. Ore Geol. Rev. 64, 23–34.

Henley, R.W., Ellis, A.J., 1983. Geothermal systems ancient and modern: a geochemical review. Earth Sci. Rev. 19, 1–50.

Hedenquist, J.W., Arribas Jr., A., Reynolds, T.J., 1998. Evolution of an intrusion-centered hydrothermal system: Far Southeast-Lepanto porphyry and epithermal Cu-Au deposits, Philippines. Econ. Geol. 93, 373–404.

Hedenquist, J.W., Arribas, R., Gonzalez-Urien, E., 2000. Exploration for epithermal gold deposits. Rev. Econ. Geol. 13, 245–277.

Hedenquist, J.W., Arribas, A., Aoki, M., 2017. Zonation of sulfate and sulfide minerals and isotopic composition in the Far Southeast porphyry and Lepanto epithermal Cu–Au deposits, Philippines. Resource Geol. 67 (2), 174–196.

Imai, A., 2000. Mineral paragenesis, fluid inclusions and sulfur isotope systematics of the Lepanto Far Southeast porphyry CuAu deposit, Mankayan, Philippines. Resource Geol. 50 (3), 151–168.

Imai, A., 2001. Generation and evolution of ore fluids for porphyry Cu-Au mineralization of the Santo Tomas II (Philex) deposit, Philippines. Resour. Geol. 51, 71–96.

Jabagat, K.D., Gabo-Ratio, J.A., Queaño, K.L., Yonezu, K., Dimalanta, C.B., Lee, Y.H., Yumul Jr., G.P., 2020. Petrogenetic constraints on magma fertility in the Baguio Mineral District, Philippines: Probing the mineralization potential of the igneous host rocks in the Sangilo epithermal deposit. Ore Geol. Rev. 103703.

Lodrigueza, L.A., Estoque, J.C., 1976. Geological report of the Masara gold and copper deposits. Apex Exploration and Mining. Unpublished internal report, 73 pp.

Malicdem, D.G., Peña, R.E., 1967. Geology of the copper-gold deposits of the Masara mine area, Mabini, Davao. In: Proceedings to the 2nd Geological Convention, Geological Society of the Philippines, vol. 2.

Malihan, T.D., Flores, R.A.L., 2012. Re-estimation of the 2011 Resource of Maco Mines located in Maco, Compostela Valley Province, Southeastern Mindanao Island, Philippines. Technical Report to the Philippine Stock Exchange, 29 pp.

Malihan, T.D., Flores, R.A.L., Ruelo, H.B., 2015. Philippine vein-type deposits: Key concepts, parameters and some examples in mineral resource/ore reserve estimation. J. Geol. Soc. Philippines 70, 3–37.

Manalo, P.C., Dimalanta, C.B., Villaplaza, B.R.B., Brown, W.W., Yumul Jr., G.P., 2017. Magnetic exploration of structurally controlled mineralization at low latitudes: A case from the Masara Gold District, Mindanao, Philippines. Econ. Geol. 112 (7), 1807–1817.

Manalo, P.C., Imai, A., Subang, L.L., de los Santos, M.C., Yanagi, K., Takahashi, R., Blamey, N.J., 2018. Mineralization of the Northwest Quartz-Pyrite-Gold Veins: Implications for multiple mineralization events at Lepanto, Mankayan Mineral District, Northern Luzon, Philippines. Econ. Geol. 113 (7), 1609–1626.

Masangcay, B.S.M., Luis, R.R.C., Irorita, K.I.N., Cellona, G.D., Maglambayan, V.B., Baluda, R.P., 2018. Mineralization controls of the gold-rich zone below Santo Tomas II porphyry copper-gold deposit, Tuba, Benguet, Philippines. J. Geol. Soc. Philippines 20, 5–11.

Mercado, A., Estoque, J.C., Lodrigueza, L.A., Ribillion, F.C., 1987. Geology and ore deposits of Masara mine, Davao del Norte. In: Proceedings of the Pacific Rim Congress '87, Australasian Institute of Mining and Metallurgy, Victoria, pp. 329–332.

Mitchell, A.H.G., Leach, T.M., 1991. Epithermal Gold Systems in the Philippines: Island Arc Metallogenesis. Geothermal Systems and Geology. Academic Press, London, p. 457.

Nagao, K., Itaya, T., 1988. K-Ar age determination. Memoir Geol. Soc. Japan 29, 5–21 (in Japanese with English abstract).

Nagao, K., Nishido, H., Itaya, T., Ogata, K., 1984. An age determination by K-Ar method. Bull. Hiruzen Res. Inst., Okayama University of Science 9, 19–38 (in Japanese with English abstract).

Pubellier, M., Deffontaines, B., Quebral, R., Rangin, C., 1994. Drainage network analysis and tectonics of Mindanao, southern Philippines. Geomorphology 9, 325–342.

Quebral, R., Pubellier, M., Rangin, C., 1996. The onset of movement on the Philippine Fault in eastern Mindanao: A transition from a collision to strike-slip environment. Tectonics 15, 713–726.

Reed, S.J.B., 1995. Electron Microprobe Microanalysis. In: Potts, P.J., Bowles, J.F.W., Reed, S.J.B., Cave, M.R. (Eds), Microprobe Techniques in the Earth Sciences, The Mineralogical Society Series 6, pp. 49–90.

Reyes, A.G., 1990. Petrology of Philippine geothermal systems and the application of alteration mineralogy to their assessment. J. Volcanol. Geoth. Res. 43, 279–309.

Reed, S.J., 2000. Quantitative trace analysis by wavelength-dispersive EPMA. Microchim. Acta 132, 145–151.
Sajona, F.G., Bellon, H., Maury, R.C., Pubellier, M., Quebral, R.D., Cotton, J., Bayon, F.E., Pagado, E., Pamatian, P., 1997. Tertiary and Quaternary magmatism in Mindanao and Leyte (Philippines): Geochronology, geochemistry and tectonic setting. J. Asian Earth Sci. 15, 121–153.
Simmons, S.F., White, N.C., John, D.A., 2005. Geological characteristics of epithermal precious and base metal deposits. Economic Geology 100th Anniversary Volume, 485–522.
Sonntag, I., Kerrich, R., Hagemann, S.G., 2011. The geochemistry of host arc volcanic rocks to the Co-o epithermal gold deposit, Eastern Mindanao, Philippines. Lithos 127, 564–580.
Steiger, R., Jager, E., 1977. Subcommission on geochronology: Convention on the use of decay constants in geo- and cosmochronology. Earth Planet. Sci. Lett. 36, 359–362.
Suerte, L.O., Imai, A., Nishihara, S., 2009. Geochemical characteristics of intrusive rocks, Southeastern Mindanao, Philippines: implication to metallogenesis of porphyry copper-gold deposits. Resour. Geol. 59, 244–262.
Tassinari, C.C.G., Pinzon, F.D., Ventura, J.B., 2008. Age and sources of gold mineralization in the Marmato mining district, NW Colombia: a Miocene–Pliocene epizonal gold deposit. Ore Geology Reviews 33 (3–4), 505–518. https://doi.org/10.1016/j.oregeorev.2007.03.002.
Tauson, V.L., Pastushkova, T.M., Bessarabova, O.I., 1998. On the limit and speciation of gold in hydrothermal pyrite. Geol Geofiz 39, 924–933.
Vikentyev, I.V., 2015. Invisible and microscopic gold in pyrite: Methods and new data for Massive sulfide ores of the Urals. Geol. Ore Deposits 57, 237–265.
Villaplaza, B.R.B., Buena, A.E., Pacle, N.A.D., Payot, B.D., Gabo-Ratio, J.A.S., Ramos, N. T., Dimalanta, C.B., Queaño, K.L., Yumul Jr., G.P., Yonezu, K., 2017. Alteration and lithogeochemistry in the Masara gold District, Eastern Mindanao, Philippines, as tools for exploration targeting. Ore Geol. Rev. 91, 530–540.
Wang, L., Qin, K.Z., Song, G.X., Li, G.M., 2019. A review of intermediate sulfidation epithermal deposits and subclassification. Ore Geol. Rev. 107, 434–456.
Waters, P.J., Cooke, D.R., Gonzales, R.I., Phillips, D., 2011. Porphyry and epithermal deposits and $^{40}Ar/^{39}Ar$ geochronology of the Baguio district, Philippines. Econ. Geol. 106, 1335–1363.
Yagi, K., 2006. Manual of mineral separation for K-Ar age dating. Engineering Geology of Japan No. 0. In: The Special Issue of the 10th Anniversary of Hiruzen Institute for Geology and Geochronology, pp. 19–25 (in Japanese).
Yumul Jr., G.P., Dimalanta, C.B., Maglambayan, V.B., Tamayo Jr., R.A., 2003. Mineralization controls in island arc settings: Insights from Philippine metallic deposits. Gondwana Res. 6, 767–776.
Yumul Jr., G.P., Brown, W.W., Dimalannta, C.B., Ausa, C.A., Faustino-Eslava, D.V., Payot, B.D., Ramos, N.T., Lizada, A.N., Buena, A.E., Villaplaza, B.R., Manalo, P.C., Queaño, K.L., Guotana, J.M.R., Pacle, N.A.D., 2017. Adakitic rocks in the Masara gold-silver mine, Compostela Valley, Mindanao, Philippines: different places, varying mechanisms? J. Asian Earth Sci. 147, 45–55.
Yumul Jr., G.P., Dimalanta, C.B., Gabo-Ratio, J.A.S., Armada, L.T., Queaño, K.L., Jabagat, K.D., 2020. Mineralization parameters and exploration targeting for gold–copper deposits in the Baguio (Luzon) and Pacific Cordillera (Mindanao) Mineral Districts, Philippines: A review. J. Asian Earth Sci. 104232.